Surface Film Characterization from X-to-K-Band Radar Signal Inversion, a Wind-Wave-Pool Experiment

Aymeric Mainvis, Vincent Fabbro, Christophe Bourlier, Henri-Jose Mametsa, Pierre Borderies

Progress In Electromagnetics Research B, Vol. 87, 93–110, 2020

Surface Film Characterization from X-to-K-Band Radar Signal Inversion, a Wind-Wave-Pool Experiment

Aymeric Mainvis[1, *], Vincent Fabbro[1], Christophe Bourlier[2], Henri-Jose Mametsa[1], and Pierre Borderies[1]

Abstract—This paper describes an experiment in a wind-wave pool in Brest, France, to characterize surface films when observed at moderate incidence from X-to-K radar bands. Measurements of the radar backscattered field were carried out for various seawater surface states and incidence angles. From this meaningful database (mainly lying in simultaneous acquisitions in X-, Ku-, and K-bands), an inversion method is proposed to characterize the elasticity modulus of the surface film. This process is based on the minimization of the cost function correlating the values given by a physical model of the damping ratio and the measured ones. The resulting oil parameters are found in overall good agreement — but still qualitative — with the various released oils. Nonetheless, the inversion method does not work properly for the rapeseed oil slick when higher wind speeds are considered, and this failure is explained. In addition, it can be seen that the results can be applied in an ocean context by comparing the modeled normalized radar cross section (NRCS) in an ocean context (given by the Bragg scattering and the Elfouhaily spectrum) and the measured NRCS.

1. INTRODUCTION

Both civil authorities and oil companies make use of either space borne or airborne remote sensing sensors to monitor hydrocarbons in an offshore context [1, 2]. This maritime activity relies, in particular, on preventing boats from illegal fuel releases and on tracking incidents. This global monitoring is also applied in the prospecting field to identify natural occurrences of crude oils on the ocean surface and so, potential natural crude oil tanks under the seafloor [3]. Currently, Synthetic Aperture Radar (SAR) is the main system used to detect hydrocarbons on sea surfaces [4–6]. This approach is preferred for weather-and-time-related issues, ensuring an anytime ready system. Electromagnetic (EM) waves are sensitive to the sea surface roughness variations induced by the presence of surface films. Precisely, the latter dampens the short sea waves by both suppression of wave growth and increase in wave dissipation [7]. This phenomenon induces zones of reduced backscatter in the SAR image which makes the presence of hydrocarbons detectable in radar imagery. Many studies have been achieved to further develop hydrocarbons detection strategies in an ocean context [1, 2, 8].

However, in a global maritime environment supervision, identifying oil-covered ocean areas is not enough. The characterization of the detected product is a key element in the decision making process for economic purposes or clean-up operations. To address this issue, optical hyperspectral imaging is commonly used [9] but remains unsatisfying in an operational monitoring context. Achieving this characterization through radar signals would be a great improvement for the supervision of oil spills. The radar signature of an oil-covered ocean surface has been tackled by many studies [10–16]. Literature depicts this particular signature thanks to theoretical models and experimental measurements from C-

Received 6 January 2020, Accepted 26 April 2020, Scheduled 9 May 2020
* Corresponding author: Aymeric Mainvis (Aymeric.Mainvis@onera.fr).
[1] ONERA/DEMR, Universite de Toulouse, Toulouse F-31055, France. [2] IETR, Polytech Nantes, Nantes, France.

to Ka-bands in both dual-polarization and cross-polarization. Precisely, the surface film (either mineral spill or biogenic slick) is studied by observing the wave damping effect.

Motivated by the previous analysis (summed up in [7]) about the impact of the wave damping effect on the radar damping ratio (which is the ratio between the clean ocean surface radar signature and the oil-covered one), this paper addresses the surface film characterization feasibility by using multi-frequency and multi-polarization data for a given illuminated controlled oil-covered seawater surface. The originality of this paper is based, firstly, on the achieved experiment providing multi-parametric and controlled-environment data of three different oils, two mineral ones: crude oil and diesel oil (forming a spill over the surface); and a biogenic one, rapeseed oil (creating a slick). The parameters are the wind speed, the incidence angle, the radar frequency and the polarization. Moreover, the seawater surface — controlled thanks to the axial fans for the wind-driven waves, the pool and the continuous oil injection over the surface — is characterized by the radar system. Secondly, the use in the surface film characterization of a physical modeling of the backscattered EM signal and the impact of the surface film on the surface is combined with a cost function minimization to estimate *a priori* the surface film chemical parameters.

This paper is organized as follows: Section 2 describes the experimental setup; it is composed of the wind-wave pool, the axial fans and the radar system. Section 3 details the radar measurement by introducing the collected database, the procedure to estimate the EM incoherent field, the damping ratio and the calibration to obtain the NRCS. The conversion of the results into the ocean context is tested in Section 4 by comparing the modeled NRCS in an ocean context (given by the Bragg scattering and the Elfouhaily spectrum) and the measured NRCS. In Section 5, the methodology to characterize the surface film is explained. The results of the suggested characterization method are displayed in Section 6 and discussed in Section 7. Finally, Section 8 is devoted to the summary and the outlooks.

2. EXPERIMENTAL SETUP

The experiment is carried out in a pool at the CEDRE[†] in Brest, France. The pool is a 20-meter-long, 11-meter-wide and 2-meter-deep seawater tank with buoys along two sides of the pool as represented in Figure 1.

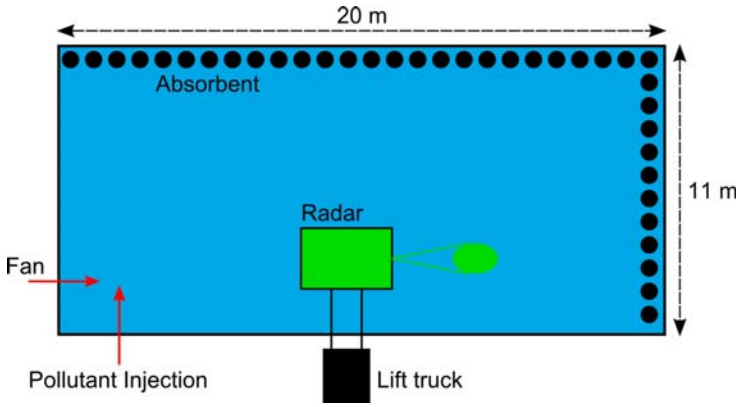

Figure 1. Schematic top view of the experimental configuration.

The steady winds are generated thanks to two axial fans sequentially used, one with a unique delivered power (left one in Figure 2) and the other one with an adjustable delivered power (right one in Figure 2). The generated airflow is constant during an experiment and the three considered different wind speeds generated by the fans are 2 m/s, 5 m/s and 8 m/s. These values are estimated thanks to an anemometer located one meter to the right of the radar system at 30 cm above the surface. It should be noted that this information does not claim to be directly related to an ocean parameter such as the wind friction or the equivalent wind speed at 10 m above the surface.

[†] Centre of Documentation, Research and Experimentation on Accidental Water Pollution

(a) (b)

Figure 2. View of the two fans, (a) TROTEC TTW 45000: 2 m/s and (b) TROTEC TTW 100000: 5 m/s and 8 m/s.

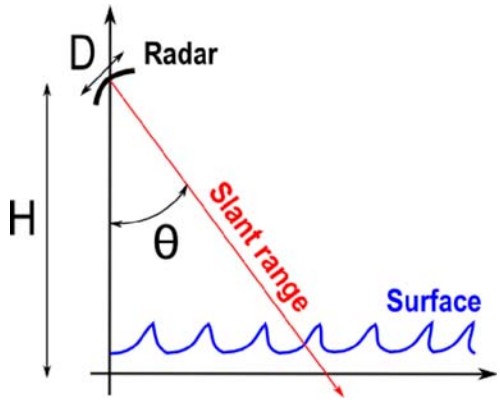

Figure 3. Schematic view of the experimental configuration.

Figure 4. Surface cleaning pump.

The radar system is set up at a fixed position 9 m to the left of the pool in Figure 1. It is plugged on two rotating plates, each one driven by a step-by-step engine (allowing inclinations up to $\pm 45^\circ$ away from nadir and possibly sweeping $\pm 180^\circ$ in azimuth). The radiofrequency (RF) signal — both the source and the receiver — is provided by a four-port vector network analyzer (VNA[‡]). The antenna is a paraboloid one described in [17], its shortest dimension is $D = 40$ cm and a bipolar source — providing measurements in polarizations V and H — is located at its focus (cf. Figure 3). In laboratory conditions, for the given antenna and for the considered radar frequencies (that are X-, Ku- and K-bands), the far-field-region condition is not achieved. Thus, the radar measurements are operated in the near-field Rayleigh region of the antenna, area where the plane wave condition exists that induces a constant incidence angle across the radar beam footprint. At nadir, the antenna is $H = 2.3$ m high above the seawater surface. At this elevation and by considering an incidence angle θ, the divergence of the beam can be neglected for the Ku- and K-bands and the distribution of the electric field is assumed to be uniform across the aperture. Indeed, the Fresnel zone starts at $D^2/2\lambda_0 \approx 3.20$ m with λ_0 the radar wavelength for a frequency of 12 GHz. This distance is qualitatively similar to $H/\cos\theta \approx 3.25$ m for $\theta = 45^\circ$. Furthermore, by considering an incidence angle of 25°, this value becomes 2.54 m and so, the measurements at frequencies greater than 12 GHz remain in the near-field Rayleigh region of the antenna. In the X-band configuration, the radar system operates in the limit of the Fresnel zone. However, the antenna is composed of a high precision offset parabolic reflector, avoiding the

[‡] ZVA from Rhode & Schwarz

divergence of the near-field beam in this controversial band. This is confirmed by the measurements of the normalized incoherent field that are continuous from 8.5 up to 23.5 GHz (cf. Appendix A). Radar absorbing materials conveniently placed aim at avoiding spurious reflections provided by whatever element of the experimental environment other than the seawater surface, remaining spurious being tackled by processing as explained further. At last, the overall RF system is installed on a lift truck.

3. RADAR MEASUREMENT

3.1. Overview of the Database

For a given wind speed, the studied oil is progressively and continuously injected on the seawater surface. It has to be mentioned that a high surplus of rapeseed oil is used to be sure that the slick is well spread on the radar footprint. The two other substances are easily spilled over the surface and so, they are not injected in a high surplus amount. The radar measurements are performed in downwind configuration at two possible incidence angles (25° and 45°) in monostatic configuration and at preselected frequency bands for co-polarizations (horizontal and vertical). The radar system is monitored by a PC — thanks to a program in Python language — controlling the motors for the antenna positioning and the VNA (Vector Network Analyzer) through an Ethernet link. After each performed measurements over the given oil-covered surface and before changing the oily substance, the pool is cleaned up thanks to the CEDRE equipment, that are two surface cleaning pumps (Figure 4) and oil-absorbent towels (Figure 5).

Figure 5. Oil-absorbent towels.

The measurements are summed up in Table 1. It should be noted that the measurements, although exhaustive, remain inhomogeneous (wind speed, incidence angle and frequency band) according to the different products due to time constraints to carry out the experiment.

Table 1. Synthesis of performed radar measurements and associated conditions.

Product	Wind Speed (m/s)	Incidence Angle (°)	Band
Seawater	2; 5; 8	25; 35; 45	X, Ku, K
Rapeseed Oil	2; 5; 8	25; 45	X, Ku, K
Crude Oil	2	45	X, Ku
Diesel Oil	5; 8	25; 45	X, Ku, K

3.2. Measurement of the Incoherent Field

Seawater surface is a specific radar target. Indeed, to measure such a moving target with the method herein, the surface has to be considered as static during the measurement time. Transmission and reception of the electromagnetic wave are achieved through the S_{11} and S_{12} ports of the VNA. Classically,

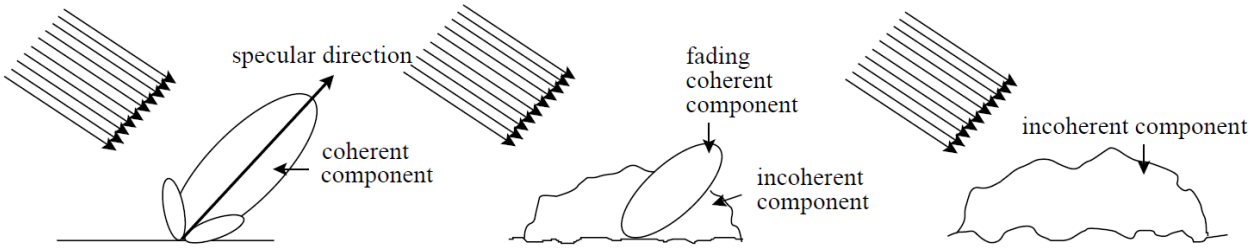

Figure 6. Evolution of the scattering according to the surface roughness [32].

to obtain range discrimination, a frequency ramp is emitted and the complex backscattered data are transformed to the time domain applying a Fourier transform. For each frequency, the time measurement duration is of order $1/B$ with B the intermediate frequency (IF) filter width. Here, the IF filter width is 100 kHz, then each radar acquisition duration is about 10 µs and the illuminated scene is assumed static during this time of acquisition. Actually, the processing in range involves a set of frequencies whose corresponding acquisition time is still fast enough so that the emitter-receiver sees a motionless scene. To provide data in the three considered frequency bands, the total EM backscattered field E_T is measured for every frequency component in the frequency ramp of the radar pulse signal (7274 frequency steps from 8 to 24 GHz). The data are then transformed to time domain in 1-GHz sub-bands, assuming that the sum of time measurements for each frequency sub-band does not exceed the backscattered field temporal coherence. In other words, the last assumption suggests a backscattered field temporal coherence greater than 4.55 ms, which is consistent with [18]. The total field E_T is estimated from 500 successive measurements m_n separated in time by 1.5 s, assuming that the seawater surface elevation at each measurement corresponds to an independent realization of the same random process. This assumption is true when the time lag is of the order of few seconds, duration much larger than the period of dominant waves [19]. The data are then incoherently averaged to derive the incoherent field E_i

$$\begin{cases} E_T = \langle m_n m_n^* \rangle \\ E_i = E_T - \langle m_n \rangle \langle m_n \rangle^* . \end{cases} \tag{1}$$

Indeed, in the case of a rough surface, the backscattered field is given by the incoherent field as shown in Figure 6. In this process, echoes from potential static targets are directly filtered; they have no variance in time. Figure 7 plots the incoherent backscattered field with an incidence angle $\theta = 45°$ in VV polarization at 10.5 GHz. The red color line is the incoherent backscattered field E_i of the seawater surface with the measured wind speed of 2 m/s. The blue dashed line is the one of the seawater surface when the fan is not powered, that is the one of a flat seawater surface. In the first case (red), the situation is similar to the one on the right side of Figure 6, the measured surface is rough and so the incoherent field exists. Then it provides a peak at a specific slant range of 3.4 m. In the second case (blue), the surface is flat and the situation is similar to the one on the left side of Figure 6, the incoherent field does not exist and the EM field is propagating in the specular direction, so the curve is flat and it corresponds to the noise level. The specific slant range of 3.4 m is given by the geometry of the experimental configuration (Figure 3). The slant range R where the antenna footprint starts is given by $R = H/\cos\theta$ with H the height of the antenna above the measured surface and θ the incidence angle. Here, the antenna is located at 2.3 m high above the seawater surface and the considered incidence angle is 45° so the slant range of the antenna footprint is about 3.25 m. The error of 15 cm is due to a lack of precision on the height of the antenna (H should be 2.4 m to get the same slant range, i.e., an error of 10 cm on the height) or on the incidence angle (θ should be 47° to get the same slant range, i.e., an error of 2°). Also, the measured sensitivity from Figure 7 is 18 dB. Typically, with a wind speed of 2 m/s and an incidence angle of 45°, the measured sensitivity is varying from 5 dB in HH polarization at 23.5 GHz to 21 dB in VV polarization at 8.5 GHz. This value is even greater when higher wind speeds and/or smaller incidence angles are considered.

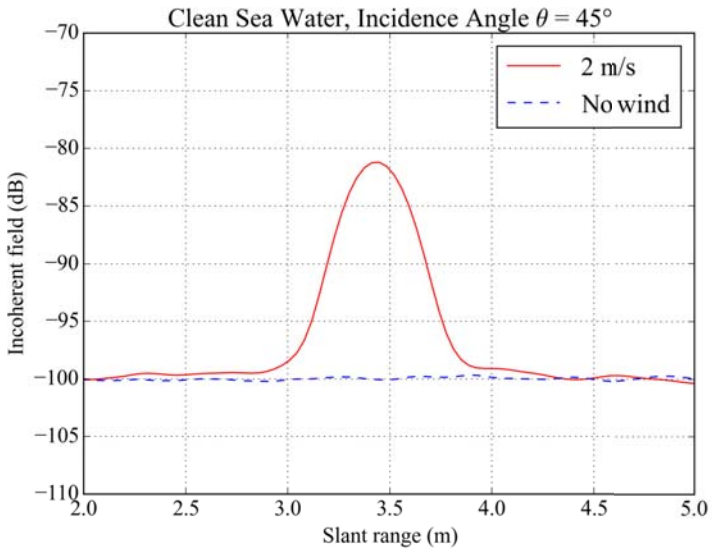

Figure 7. Incoherent field of the clean seawater surface with an incidence angle of 45° in VV polarization at 10.5 GHz. Two configurations are observed: a seawater state with a wind speed of 2 m/s (red line) and a flat seawater surface (blue dashed line).

3.3. Measurement of the Damping Ratio

The damping ratio β is defined as the ratio between the RCS (or either the NRCS since it is a ratio) of a clean seawater surface σ_c and the one of a polluted surface σ_p, that is $\beta = \sigma_c/\sigma_p$. The RCS is proportional to the intensity of the incoherent backscattered field. More precisely, it corresponds to the mean value of the incoherent backscattered field over the radar beam footprint on the seawater surface [19]. To get a measurement statistically representative of the random seawater surface elevation, the footprint size has to be much larger than the dominant wavelength of the studied surface. In experimental conditions, the

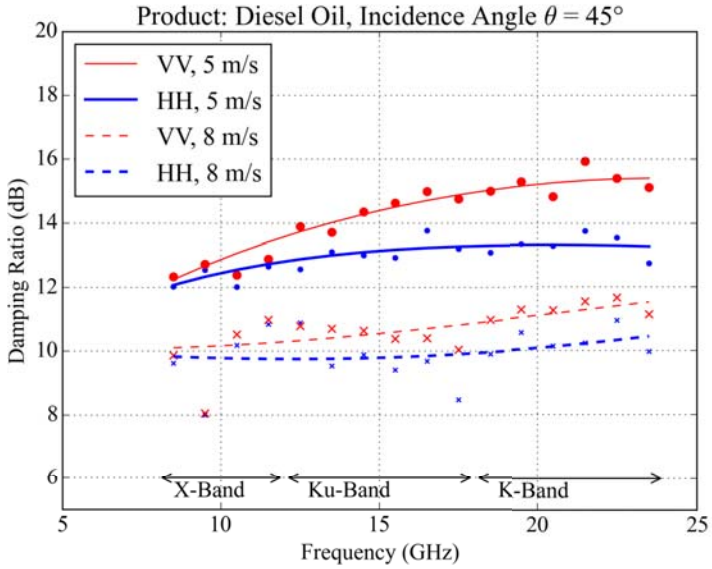

Figure 8. Damping ratios from the diesel oil spill acquired at two different wind speeds (5 and 8 m/s) in VV (red) and HH (blue) polarizations with an incidence angle of 45°. The lines are third-degree-polynomial fits on the acquired data points (dots and crosses).

measured 3 dB footprint size S_p is ≈ 19.5 cm for $\theta = 25°$ and ≈ 27.0 cm for 45°. However, the missing large scales are included through their tilting effect in the time-averaging process of the backscattered field [19].

Figure 8 shows an example of measured damping ratios from the diesel oil spill considering two different wind speeds in VV and HH polarizations with an incidence angle of 45°. One can observe that the damping ratio increases from X- to K-bands and decreases with increasing the wind speed. These observations are in agreement with those summed up by [7]. However, the damping ratio is impacted by the polarization in Ku- and K-bands. This difference claims a non-negligible dielectric effect at higher frequency bands (K-band in particular). Nevertheless, it remains minor in comparison to the roughness changes [20]. Moreover, this effect decreases with increasing the surface state, retrieving the conclusion described by [7] in an ocean context.

3.4. Calibration Procedure

The backscattering coefficient can be obtained from the measurements of the incoherent electromagnetic field thanks to the calibration procedure. On one hand, as previously said in Section 2, the EM field is assumed to be uniform across the aperture since the seawater surface is in the near-field region of the antenna. On the other hand, the incoherent backscattered field received on the antenna is in the far field of the ripples of the surface. The radar equation applied to this configuration gives the following backscattered power P_r received by the antenna

$$P_r = P_i A_w \sigma_0 \frac{\eta}{4\pi D_w^2}, \tag{2}$$

where P_i is the emitted power, $A_w = A_a/\cos\theta$ is the area of the seawater surface which is illuminated by the antenna beam with an incidence angle θ, σ_0 is the NRCS of the seawater surface, η is the antenna efficiency, A_a is the antenna surface and D_w is the distance between the antenna and the water surface. Let us now consider a reference target, a trihedral corner reflector with a known radar cross section σ_t at a distance D_t from the antenna (the antenna is in the far-field region of the corner reflector). Therewith, the received power P_t is

$$P_t = P_i \sigma_t \frac{\eta}{4\pi D_t^2}, \tag{3}$$

and so the NRCS is given by

$$\sigma_0 = \frac{P_r}{P_t} \frac{D_w^2}{D_t^2} \frac{\sigma_t}{A_w}. \tag{4}$$

The measurement of the reference power P_t is done with a 10 cm edge corner reflector and its known radar cross section is

$$\sigma_t = \frac{4\pi e^4}{3\lambda_0^2}, \tag{5}$$

where e is the edge length and λ_0 is the EM wavelength.

4. OCEAN TRANSPOSITION

4.1. Bragg Scattering Mechanism

The Bragg theory predicts that the NRCS is proportional to the spectral energy density of the Bragg waves, that are the sea surface waves of wavenumber k_B [14],

$$k_B = 2k_0 \sin\theta, \tag{6}$$

with $k_0 = 2\pi/\lambda_0$ the radar wavenumber, λ_0 the radar wavelength and θ the incidence angle. By considering a seawater surface with a wavenumber spectrum S_k, the NRCS σ_0 is given by [21]

$$\sigma_0(k_0, \theta) = \frac{1}{4k_0} \left|\mathbb{B}(k_0, \theta)\right|^2 S_k(k_B), \tag{7}$$

where $\mathbb{B}(k_0, \theta)$ is the first order small perturbation model kernel, a term driven by the polarization and the dielectric characteristics.

4.2. Pool to Ocean Transposition

Let us assume that the measured backscattering coefficient σ_{pool} is fully described by the Bragg scattering mechanism,

$$\sigma_{\text{pool}}(k_0, \theta) = \frac{1}{4k_0} |\mathbb{B}(k_0, \theta)|^2 S_{\text{pool}}(k_B), \tag{8}$$

where S_{pool} is the spectrum of the seawater surface in the pool. This assumption is usually made to interpret the ocean features in SAR data [22, 23] and here, the non-polarized radar returns from breaking waves are considered negligible. This NRCS can be compared with the NRCS in an ocean context σ_{ocean} such as

$$\sigma_{\text{pool}}(k_0, \theta) = \Delta(k_B)\sigma_{\text{ocean}}(k_0, \theta) = \frac{1}{4k_0} |\mathbb{B}(k_0, \theta)|^2 \Delta(k_B) S_{\text{ocean}}(k_B), \tag{9}$$

where Δ is the deviation function depending on k_B and S_{ocean} is the sea spectrum. From these relations, the expression linking the structure of the surface of the pool to that of the ocean is therefore

$$S_{\text{pool}}(k_B) = \Delta(k_B) S_{\text{ocean}}(k_B), \tag{10}$$

and the following pool-to-ocean-transposition criterion is defined such as

$$\Delta(k_B) \approx \text{cst}. \tag{11}$$

Actually, this criterion reflects a similar structure between the two surfaces over the measured EM frequency range.

This criterion is tested on the measurements as shown in Figure 9, Figure 10, and Figure 11. The measured NRCS is compared with the modeled NRCS in Eq. (7) by using the Elfouhaily spectrum [24] to describe the structure of the ocean surface. The deviation function Δ is estimated thanks to Eq. (9)

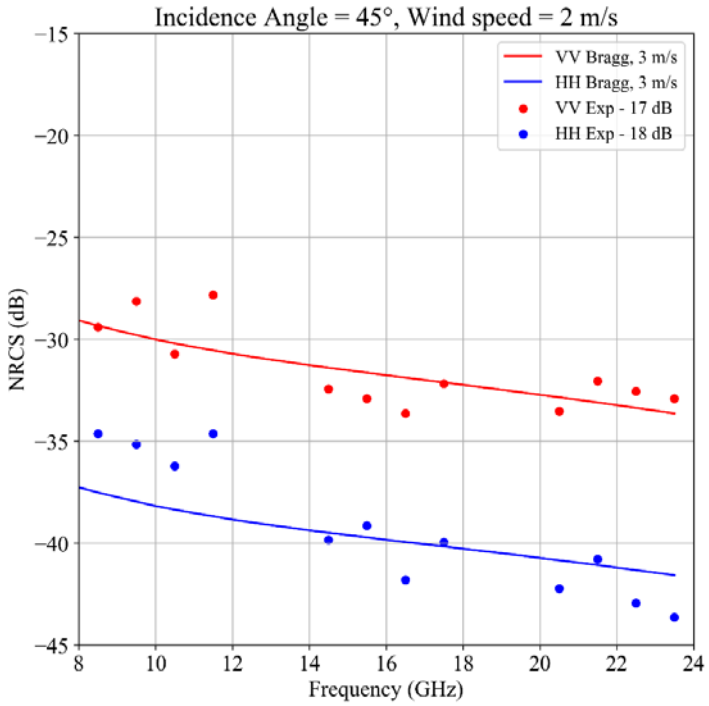

Figure 9. Comparison between the measured NRCS in the pool (dots) and the modeled NRCS with the Elfouhaily spectrum for a wind speed at 10 m above the sea surface of 3 m/s (continuous curve) in dB. The experimental conditions are: an incidence angle of 45° and a wind speed of 2 m/s. The VV polarization is in red color and the HH one in blue color. The mean value of the deviation function Δ over the EM frequency range is subtracted from the measured NRCS.

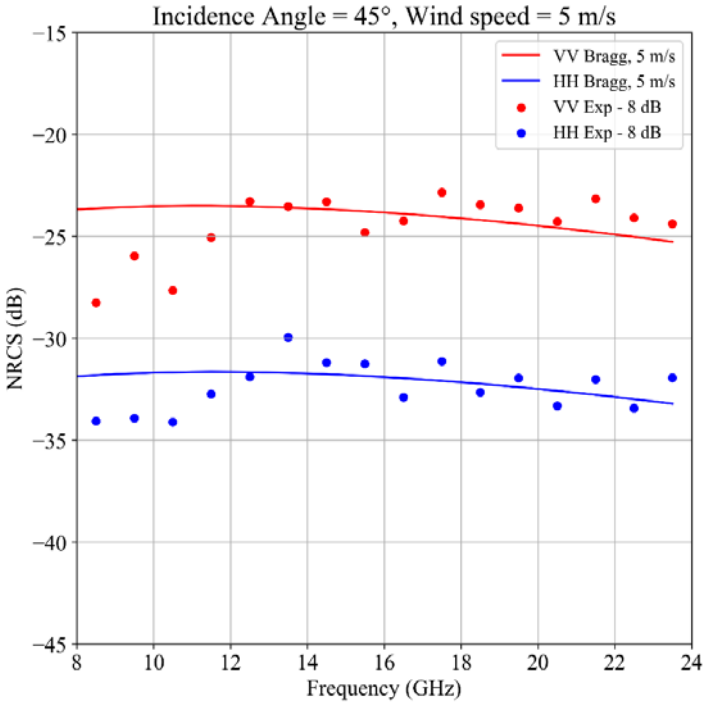

Figure 10. Comparison between the measured NRCS in the pool (dots) and the modeled NRCS with the Elfouhaily spectrum for a wind speed at 10 m above the sea surface of 5 m/s (continuous curve) in dB. The experimental conditions are: an incidence angle of 45° and a wind speed of 5 m/s. The VV polarization is in red color and the HH one in blue color. The mean value of the deviation function Δ over the EM frequency range is subtracted from the measured NRCS.

and then its mean value is subtracted from the measured NRCS. The deviation function is almost constant over the frequency range with variations of ±2 dB except for the X-band (±3 dB). Here, the measured wind speed is treated as the wind speed at 10 m above the ocean surface (u_{10}) to estimate the modeled NRCS except for Figure 9 with a wind speed of 2 m/s, the Elfouhaily spectrum is not defined for $u_{10} < 3$ m/s. One can see that the measurements and the modeling are in good agreement with a same frequency behavior.

This shows that the structure of the capillarity waves of the pool are similar to those of the modeled ocean (but more energetic since $\Delta > 0$) and the structure of the larger waves (measured by the lower EM frequencies) tends to differ from that of the modeled ocean. This result is consistent with the experimental conditions since the pool has finite dimensions and the fetch is limited, therefore the larger waves of the pool cannot be similar to those of the ocean. However, the difference for the X-band remains quantitatively acceptable and then, the pool-to-ocean-transposition criterion can be considered valid over the measured frequency range. Therewith, the observations recorded in the pool are representative of the corresponding oceanic phenomena **only** in the simplified context described by the Elfouhaily model and the Bragg scattering.

5. OIL FILM CHARACTERIZATION

5.1. Overview of the Methodology

The objective is to correlate the measured damping ratios with a surface film characterization. To do this, the suggested approach is based on the Bragg scattering mechanism and on the modeled damping ratio proposed by [11]. In the Bragg scattering regime, the NRCS is expressed as the multiplication between the Bragg kernel — corresponding to an effect mainly driven by the polarization and by the dielectric characteristics — and the wavenumber spectrum. This asymptotic formalism is called the first

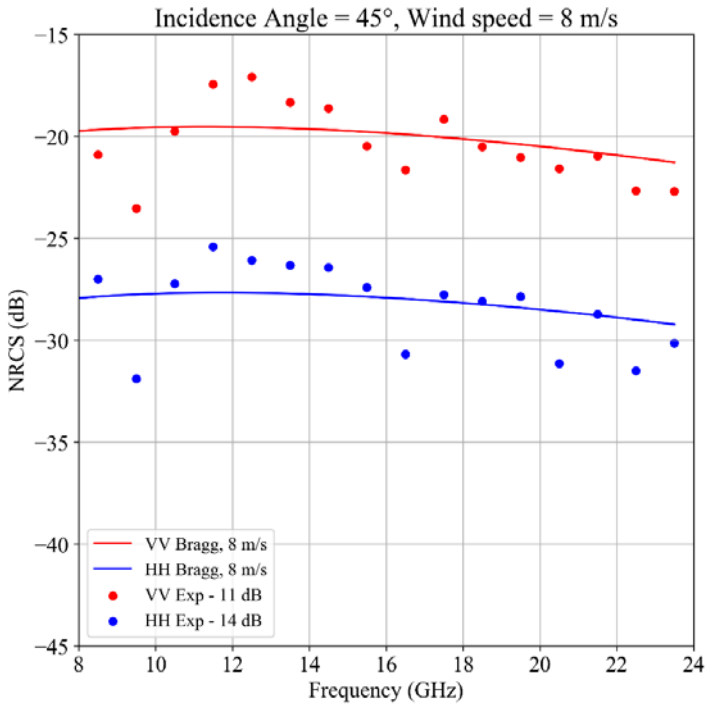

Figure 11. Comparison between the measured NRCS in the pool (dots) and the modeled NRCS with the Elfouhaily spectrum for a wind speed at 10 m above the sea surface of 8 m/s (continuous curve) in dB. The experimental conditions are: an incidence angle of 45° and a wind speed of 8 m/s. The VV polarization is in red color and the HH one in blue color. The mean value of the deviation function Δ over the EM frequency range is subtracted from the measured NRCS.

order small perturbation method (SPM1). The modeled damping ratio is applied to the wavenumber spectrum of the clean surface to characterize the damping effect provided by a given surface film. In this modeled ratio, three main parameters are used to describe the surface film: the elasticity modulus E_0 in N/m, the characteristic pulsation related to intermolecular forces ω_D in rad/s and the fractional filling factor F. From the Bragg scattering regime and with some approximations discussed later in the paper, the damping ratio can be directly derived from the NRCS ratio between clean and contaminated sea surfaces. Afterwards, a cost function minimization is applied on the measured damping ratios to get the three parameters $\{\omega_D, E_0, F\}$ from the modeled damping ratio.

5.2. Damping Ratio Modeling

By applying the Bragg scattering theory, the EM damping ratio β is linked to the wave damping ratio y_s such as

$$\beta = \frac{\sigma_c}{\sigma_p} = \frac{S_{k,c}(k_B)}{S_{k,p}(k_B)} = y_s, \tag{12}$$

where $S_{k,c}$ is the clean surface spectrum and $S_{k,p}$ is the spectrum of the polluted surface. Here, the oil dielectric impact is neglected in the kernel $\mathbb{B}(k_0, \theta)$. Indeed, oils are dielectric media with low relative permittivity and low loss factor. At microwave frequencies, the average relative permittivity ε' ranges between 2.2 and 2.3 and the loss factor ε'' is about 0.01 [25, 26]. The relative penetration depth δ for a lossy medium [27],

$$\delta = \frac{\lambda_0}{\pi\sqrt{2}\left[\sqrt{\varepsilon'^2 + \varepsilon''^2} - \varepsilon'\right]^{\frac{1}{2}}} \approx \frac{\lambda_0\sqrt{\varepsilon'}}{\pi\varepsilon''} \approx 47.75\lambda_0 \tag{13}$$

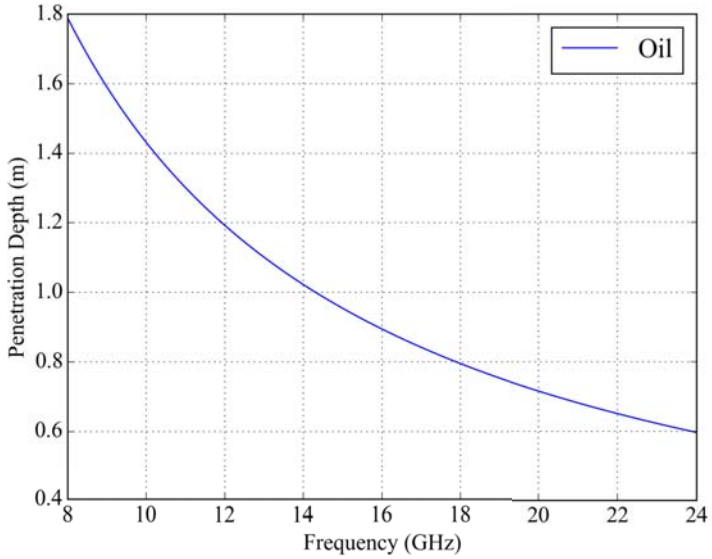

Figure 12. Oil penetration depth.

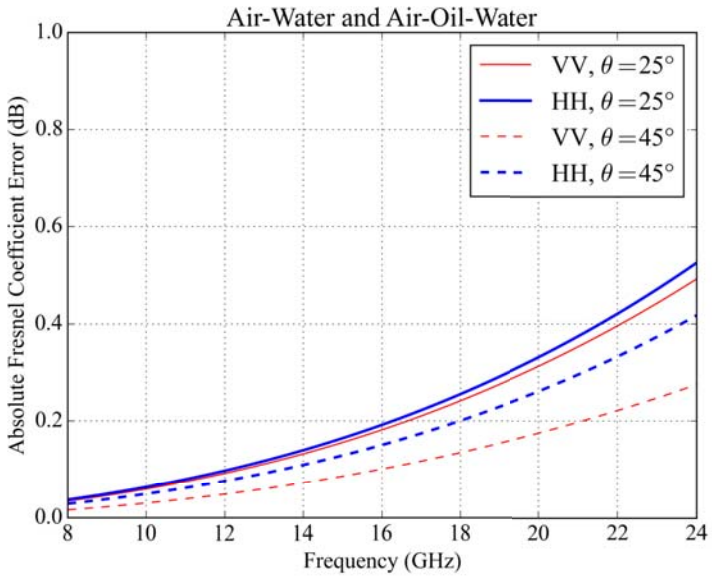

Figure 13. Absolute Fresnel reflection coefficient error with a surface film thickness of 1 mm in VV (red) and HH (blue) polarizations. The oil relative permittivity is 2.25 and the oil loss factor is 0.01. The seawater dielectric constant is computed from the Meissner and Wentz model. Two incidence angles are studied: 25° in continuous line and 45° in dashed line.

with λ_0 the radar wavelength, is plotted in Figure 12 for the X-, Ku- and K-bands ($\varepsilon' = 2.25$ and $\varepsilon'' = 0.01$). This term characterizes the energy loss within a medium. It defines the deepness reached by the EM wave into a medium such as its electric field magnitude has decreased by a factor $1/e$. In Figure 12, the minimum penetration depth is about 60 cm and it remains much greater than the studied surface film thickness (less than 1 mm). Moreover, considering the two-layer Fresnel reflection coefficients $\Gamma_{A/W}$ rather than the equivalent three-layer ones $\Gamma_{A/O/W}$ leads to a minor error as depicted in Figure 13. These coefficients describe the changes of the refractive index within the layers. The maximum absolute Fresnel reflection coefficients error on amplitude $|\Gamma_{A/W} - \Gamma_{A/O/W}|$ is about 0.5 dB with a surface film thickness equal to 1 mm for the radar frequency 24 GHz. Then, the dielectric effect

of the surface film is very low but should be considered as not negligible in the K-band when the thickness is 1 mm. However, to keep an easy-to-apply approach, this effect is not considered here and the inversion method could be improved by considering the equivalent three-layer Fresnel coefficients. The improvements will be discussed later in Section 7.

Therefore, the surface film has a very low impact on the loss of EM energy and the dielectric influence is ignored as a first approximation.

The damping ratio β previously described is equal to the wave damping ratio y_s defined for monomolecular films [11]

$$y_s(f) = \frac{1}{1 - F + F/y(f)}, \tag{14}$$

with F the fractional filling factor, i.e., the ratio of the area covered by film with respect to the total area considered, and

$$y(f) = \frac{1 \pm 2\varphi + 2\varphi^2 - X + Y(X + \varphi)}{1 \pm 2\varphi + 2\varphi^2 - 2X + 2X^2}, \tag{15}$$

with

$$\varphi = \left(\frac{\omega_D}{2\omega}\right)^{\frac{1}{2}} \quad X = \frac{E_0 k^2}{\rho(2\nu\omega^3)^{\frac{1}{2}}} \quad Y = \frac{E_0 k}{4\nu\rho\omega}, \tag{16}$$

dimensionless quantities and

$$f = \frac{\omega(k)}{2\pi}, \tag{17}$$

the dispersion relationship [24]. ω_D is a characteristic pulsation related to intermolecular forces, E_0 is the elasticity modulus, $\rho = 1.026 \cdot 10^3\,\mathrm{kg/m^3}$ the seawater density, $\nu = 1.189 \cdot 10^{-6}\,\mathrm{m^2/s}$ the seawater kinematic viscosity [11]. A plus sign in (15) refers to soluble film, whereas a minus to insoluble film. In this experiment, the surface films are considered insoluble. It should be noted that this expression does not consider the layer thickness and so, it has to be applied to thin-layer problem (which is the case for the experiment). In the thin-layer problem, the layer has an impact on the roughness of the surface but the dielectric effect is negligible. Therewith, an analytical expression of the EM damping ratio is established by considering the Bragg scattering mechanism.

5.3. Cost Function Minimization

The wave damping ratio y_s is correlated to the measured one in order to extract the characterization parameters of the illuminated surface film, that are the characteristic pulsation ω_D, the elasticity modulus E_0 and the fractional filling factor F. To do so, the minimization of the cost function $C(\omega_D, E_0, F)$ is undertaken, with

$$C(\omega_D, E_0, F) = \sum_{i=0}^{N-1} \parallel y_s(k_i) - \beta(k_i) \parallel^2, \tag{18}$$

where $\parallel \cdots \parallel^2$ is the Euclidean distance and β the measured damping ratio at the Bragg wavenumber k_i. N measured damping ratios are available corresponding to N different radar frequencies over X-, Ku-, and K-bands for a given incidence angle. Here, the wave damping ratio y_s is written as a function of the wavenumber and not of the frequency; this is possible thanks to the dispersion relationship. The minimization process is operated thanks to the Python language package *optimize* from *SciPy* providing constrained minimization of multivariate scalar functions by using two different methods: *L-BFGS-B* and *TNC*. *L-BFGS-B* is a limited-memory algorithm for solving large nonlinear optimization problems subject to simple bounds on the variables [28]. *TNC* uses a truncated Newton algorithm to minimize a function with variables subject to bounds thanks to gradient information [29]. The minimization process is constrained to ensure physical solutions [11, 13–15, 30], then ω_D is varying between 1 and 40 rad/s, the variable E_0 ranges from 1 to 50 mN/m and F from 0 to 1.

6. RESULTS

The inversion process — introduced in Section 5 — is applied to the measured damping ratios to estimate the parameters of the illuminated surface film. This strategy is successively used on the three products (crude oil, diesel oil and rapeseed oil) by regarding polarization, wind speed and incidence angle. Figure 14, Figure 15 and Figure 16 show the modeled damping ratios by using the estimated

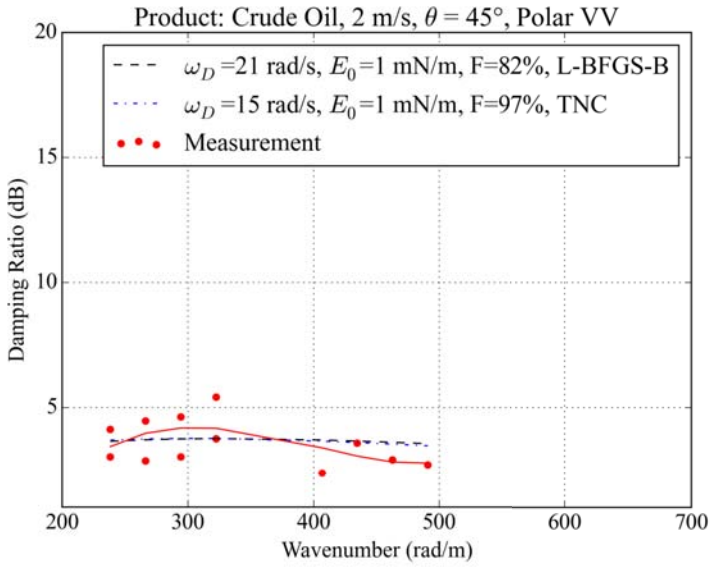

Figure 14. Damping ratios calculated for crude oil spill by considering a wind speed of 2 m/s in VV polarization for an incidence angle of 45°. The data points (red dots) are fitted by a third-degree polynomial (red line). The dashed lines are the damping ratios obtained from the minimization process (black dashed line: L-BFGS-B method, blue dotted line: TNC method).

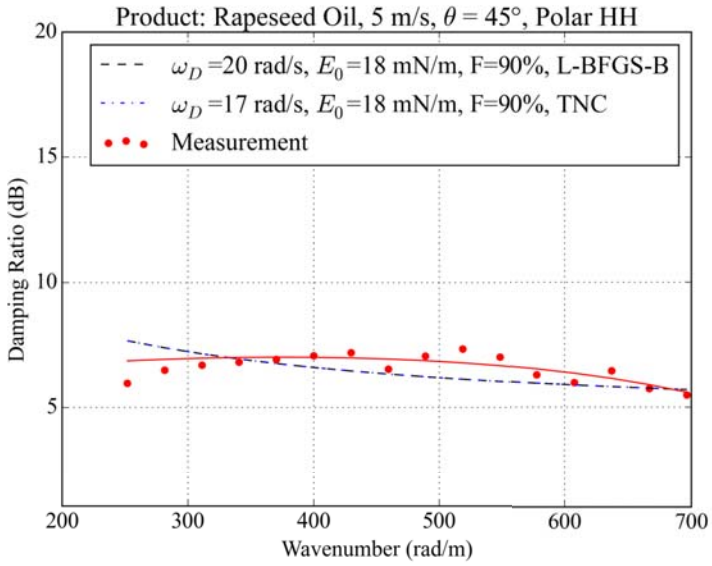

Figure 15. Damping ratios calculated for rapeseed oil slick by considering a wind speed of 5 m/s in HH polarization for an incidence angle of 45°. The data points (red dots) are fitted by a third-degree polynomial (red line). The dashed lines are the damping ratios obtained from the minimization process (black dashed line: L-BFGS-B method, blue dotted line: TNC method).

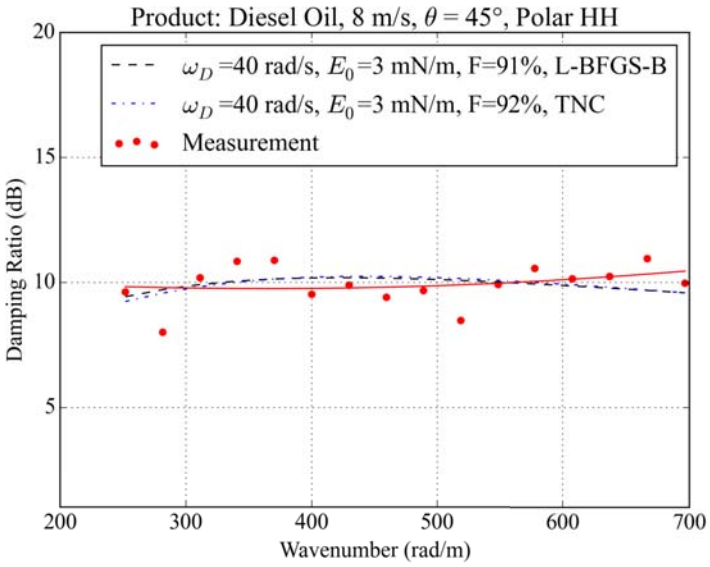

Figure 16. Damping ratios calculated for diesel oil spill by considering a wind speed of 8 m/s in HH polarization for an incidence angle of 45°. The data points (red dots) are fitted by a third-degree polynomial (red line). The dashed lines are the damping ratios obtained from the minimization process (black dashed line: L-BFGS-B method, blue dotted line: TNC method).

parameters after the cost function minimization, they are compared with the measured damping ratios. The retrieved damping ratios are qualitatively in good agreement with the measured damping ratios.

In Figure 14, the estimated elasticity modulus E_0 is 1 mN/m. Typically, this value stands for oil spills ($E_0 < 10$ mN/m) [30] and so, it is in agreement with a crude oil spill. The retrieved elasticity modulus 18 mN/m in Figure 15 shows a chemical composition different from the crude oil, which is consistent. The value 3 mN/m in Figure 16 agrees with an oil spill. In these plots, the introduced method makes a chemical-related identification possible.

Table 2 presents all the retrieved product parameters $\{\omega_D, E_0, F\}$ in {rad/s, mN/m, dimensionless quantity} after applying the cost function minimization. The first column displays the experimental conditions, which are the wind speed in m/s, the incidence angle θ in degree and the polarization VV or HH. The symbol ∅ stands for non-acquired data. Here, the focus is on the elasticity modulus, the main

Table 2. Synthesis of inverted oil characterization parameters derived from the two methods, in bold characters *L-BFGS-B* and in normal characters *TNC*. The associated conditions are indicated in the first column: wind speed, incidence angle and polarization.

Parameters	Crude Oil	Rapeseed Oil	Diesel Oil
2 m/s, 45°, VV	**[21, 1, 0.82]** [15, 1, 0.97]	**[25, 11, 1.0]** [33, 11, 1.0]	∅
2 m/s, 45°, HH	**[21, 1, 0.86]** [15, 1, 0.93]	**[22, 17, 1.0]** [22, 17, 1.0]	∅
5 m/s, 45°, VV	∅	**[40, 3, 0.91]** [40, 3, 0.90]	**[40, 3, 0.98]** [40, 3, 0.98]
5 m/s, 45°, HH	∅	**[20, 18, 0.90]** [17, 18, 0.90]	**[40, 3, 0.97]** [40, 3, 0.97]
5 m/s, 25°, VV	∅	∅	**[40, 5, 0.98]** [38, 5, 0.98]
5 m/s, 25°, HH	∅	∅	**[40, 5, 0.98]** [39, 5, 0.98]
8 m/s, 45°, VV	∅	**[40, 3, 0.91]** [31, 2, 0.95]	**[40, 3, 0.94]** [40, 3, 0.94]
8 m/s, 45°, HH	∅	**[40, 2, 0.90]** [1, 4, 1.0]	**[40, 3, 0.91]** [40, 3, 0.92]
8 m/s, 25°, VV	∅	**[40, 12, 0.90]** [40, 12, 0.90]	∅
8 m/s, 25°, HH	∅	**[40, 15, 0.90]** [40, 15, 0.90]	∅

parameter to characterize the surface film (by following the criterion $E_0 < 10\,\mathrm{mN/m}$ for an oil spill). About the crude oil and the diesel oil, the estimated elasticity modulus is very steady despite variations in the various experimental parameters with a range of variations between 1 mN/m and 5 mN/m. Moreover, these values of the elasticity modulus are consistent with the criterion $E_0 < 10\,\mathrm{mN/m}$ for an oil spill. The rapeseed oil is trickier. Indeed, the estimated elasticity modulus is between 2 and 18 mN/m which is a huge span. The value changes with the wind speed, the incidence angle and even with the polarization. The variations with the polarization are consistent with the high surplus of rapeseed oil on the surface (3.1). Therewith, the dielectric effect of the oil slick is no more negligible and so the damping ratio depends on the polarization. About the evolution with the wind speed and the incidence angle, seemingly, at higher wind speeds and unlike the diesel oil film and the crude oil film, which are spilled over the surface in a very thin layer, the rapeseed oil slick shifts from a homogeneous layer to an inhomogeneous one. So, it moves from a film to an emulsion. Then, the considered modeling of the damping ratio is not sufficient to describe the overall phenomenon. The rapeseed behavior is shown in Figure 17 with a wind speed of 2 m/s and Figure 18 with a wind speed of 8 m/s. As previously suggested, in Figure 17, the rapeseed oil slick is homogeneous with large oil bubbles while in Figure 18 the slick becomes inhomogeneous and the bubbles are difficult to identify from the seawater.

Figure 17. Photograph from the rapeseed-oil-covered seawater surface. The wind speed is 2 m/s.

Figure 18. Photograph from the rapeseed-oil-covered seawater surface. The wind speed is 8 m/s.

7. DISCUSSION

Actually, this experiment is not achieved on the open sea but on a finite open pool. Then, the experimental conditions are drastically different from the ocean ones, which are much more complex. Indeed, a realistic wind profile cannot be generated due to the finite dimensions of the pool and so, the experiment does not reproduce the wave breaking and the nonlinear interactions. Furthermore, the buoys system — along two sides of the pool — is certainly insufficient to prevent every standing waves in the pool. Consequently, this work does not claim to be fully representative of the ocean surface.

Naturally, the problem of oil-covered ocean surface is incredibly complex and may require a complement interpretation of a chemist. The case of crude oil accidents up to thicknesses of centimeters are encountered and thus, the damping mechanism within such spills changes. Moreover, after some weeks, partial photochemical and microbial transformations lead to partial formation of surface active transformation products that may be surface active and so behaving similar to biogenic slicks, i.e., the spill center may be surrounded by a large "artificial slick" area inducing a tricky damping mechanism. Nonetheless, what is truly at stake in this work is to further understand the EM backscattering from oil-covered seawater surfaces thanks to measurements acquired in a fully-controlled environment, which is definitely not achievable on the open sea.

About the suggested inversion method, it is assumed that the scattering process from the seawater surface is described by the Bragg scattering mechanism. This modeling is suitable in this experiment

but remains rarely verified in ocean conditions for near-nadir incidence angles. To keep the validity of the inversion method, the considered incidence angles have to be in the interval $[45°, 70°]$ corresponding to the validity domain of the Bragg scattering. Also, the technique could be transposed to lower radar frequencies (L-, S- and C-bands), where the modeling is certainly valid. By the way, the same methodology has been applied by [12] in ocean conditions for wind speeds between 1.5 m/s and 5 m/s in L-, S-, C-, X- and Ku-bands and for incidence angles between 23° and 65°, suggesting that the criterion of validity of the Bragg scattering remains largely too restrictive. Moreover, the thickness of the oil layer is disregarded to consider a surface film problem only and it is assumed that the oil layer is homogeneous, i.e., this is not an emulsion. These assumptions could be relaxed by adding the variations of the Bragg kernels within the inversion process. Then, thanks to the mixing law or/and the equivalent three-layer Fresnel coefficients, the emulsion rate or/and the thickness could be estimated.

At last, note that the problem of contamination on rivers by hydrocarbons is also a very actual issue, and the work presented here could be more directly applicable in this context [31].

8. SUMMARY AND OUTLOOKS

Measurements in a wind-wave pool and modeling of the wave damping ratio from oil-covered seawater surface were combined to elaborate an *a priori* oil characterization methodology over multi-frequency radar data. About physical modeling and well-controlled experiments, an extended description of the seawater surface is proposed through the radar backscatter. The characterization methodology is based on the minimization of the cost function correlating the values given by a physical modeling of the damping ratio and the measured ones. The oil characterization approach is reliable to identify the elasticity modulus of the crude oil and the diesel oil. However, the methodology does not succeed in retrieving the chemical parameters of the rapeseed oil and so it could be an error-raising vector in a blind inversion process. In an operational context, this ambiguity could be vanished by monitoring the detected surface film along different meteorological conditions.

This study shows that accurate multi-frequency radar measurements could be a relevant means to characterize an oil-covered sea surface. Then, in future works, this oil characterization methodology will be applied on other database acquired in a maritime environment to further test the resilience of the strategy by considering an operational context and numerous surface films.

ACKNOWLEDGMENT

Research presented in this paper is part of the NAOMI (New Advanced Observation Method Integration) Project funded by TOTAL (the French Oil and Gas Company) and ONERA (the French Aerospace Lab). The authors would like to thank all people involved in this project, and especially Veronique Miegebielle and Dominique Dubucq from TOTAL for supporting this work. The authors are very grateful to the CEDRE (Centre of Documentation, Research and Experimentation on Accidental Water Pollution) for allowing us to achieve the Oil-on-Water exercise, which was carried out during 25–29 September and 9–13 October, 2017.

APPENDIX A. NEAR-FIELD CONFIGURATION

As explained in Section 2, in X-band configuration the radar system operates in the limit of the Fresnel zone. This issue does not occur with higher frequencies — like 23.5 GHz for example — and the radar measurements are then achieved in the near-field region. Figure A1 plots the normalized incoherent field with respect to the slant range (cf. Figure 3) considering a clean seawater surface with a wind speed of 2 m/s and an incidence angle $\theta = 45°$ in VV polarization. The three displayed fields result from three different radar frequencies; 8.5 GHz, 11.5 GHz and 23.5 GHz. The radar beam footprints projected on the seawater surface and observed across the slant range are similar regardless of EM frequency. This result shows that no divergence of the beam occurs in X-band configuration and all of the radar measurements are therefore realized in the near-field region.

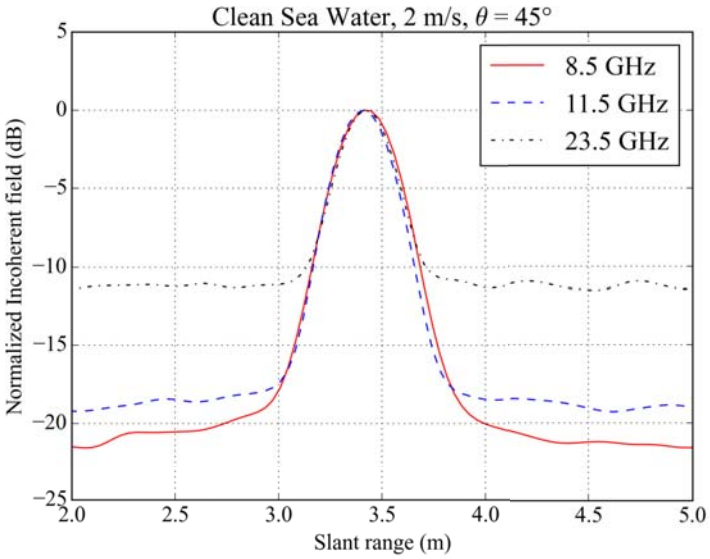

Figure A1. Normalized incoherent field of the clean seawater surface with an incidence angle 45° and a wind speed of 2 m/s in VV polarization. Three EM frequencies are shown: 8.5 GHz (red line), 11.5 GHz (blue dashed line) and 23.5 GHz (black dotted line).

REFERENCES

1. Fingas, M. and C. Brown, "Review of oil spill remote sensing," *Mar. Pollut. Bull.*, Vol. 83, 9–23, 2014.
2. Leifer, I., W. J. Lehr, D. Simecek-Beatty, E. Bradley, R. Clark, P. Dennison, Y. Hu, S. Matheson, C. E. Jones, B. Holt, M. Reif, D. A. Roberts, J. Svejkovsky, G. Swayze, and J. Wozencraft, "State of the art satellite and airborne marine oil spill remote sensing: Application to the BP Deepwater Horizon oil spill," *Remote Sens. Environ.*, Vol. 124, 185–209, 2012.
3. Jatiault, R., D. Dhont, L. Loncke, and D. Dubucq, "Monitoring of natural oil seepage in the Lower Congo Basin using SAR observations," *Remote Sens. Environ.*, Vol. 191, 258–272, 2017.
4. Gade, M. and W. Alpers, "Using ERS-2 SAR images for routine observation of marine pollution in European coastal waters," *Sci. Total Environ.*, Vols. 237–238, 441–448, 1999.
5. Girard-Ardhuin, F., G. Mercier, F. Collard, and R. Garello, "Operational oil-slick characterization by SAR imagery and synergistic data," *IEEE J. Ocean. Eng.*, Vol. 30, 487–495, 2005.
6. Garcia-Pineda, O., B. Zimmer, M. Howard, W. Pichel, X. Li, and I. R. Macdonald, "Using SAR images to delineate ocean oil slicks with a texture-classifying neural network algorithm (TCNNA)," *Can. J. Remote Sens.*, Vol. 35, 411–421, 2009.
7. Holt, B. and C. Jones, "Detection of marine slicks with SAR: Scientific and experimental legacy of werner alpers, his students and colleagues," *Int. Geosci. Remote Sens. Symp.*, 1480–1483, 2017.
8. Solberg, A. H., "Remote sensing of ocean oil-spill pollution," *Proc. IEEE*, Vol. 100, 2931–2945, 2012.
9. Angelliaume, S., X. Ceamanos, F. Viallefont-Robinet, R. Baqué, P. Déliot, and V. Miegebielle, "Hyperspectral and radar airborne imagery over controlled release of oil at sea," *Sensors*, Vol. 17, 1–21, 2017.
10. Alpers, W. and H. Hühnerfuss, "Radar signatures of oil films floating on the sea surface and the marangoni effect," *J. Geophys. Res. Ocean.*, Vol. 93, 3642–3648, 1988.
11. Lombardini, P. P., B. Fiscella, P. Trivero, C. Cappa, and W. Garrett, "Modulation of the spectra of short gravity waves by sea surface films: Slick detection and characterization with a microwave probe," *J. Atmos. Ocean. Technol.*, Vol. 6, 882–890, 1989.

12. Hühnerfuss, H., A. Gericke, W. Alpers, R. Theis, V. Wismann, and P. A. Lange, "Classification of sea slicks by multifrequency radar techniques: New chemical insights and their geophysical implications," *J. Geophys. Res.*, Vol. 99, 9835–9845, 1994.
13. Gade, M., W. Alpers, H. Hühnerfuss, and P. A. Lange, "Wind wave tank measurements of wave damping and radar cross sections in the presence of monomolecular surface films," *J. Geophys. Res.*, Vol. 103, 3167–3178, 1998.
14. Gade, M., W. Alpers, H. Hühnerfuss, H. Masuko, T. Kobayashi, "Imaging of biogenic and anthropogenic ocean surface films by the multifrequency/multipolarization SIR-C/X-SAR," *J. Geophys. Res. Ocean.*, Vol. 103, 18,851–18,866, 1998.
15. Ermakov, S. A., "Possibilities of identification of oil films using radar probing of the sea surface," *US/EU-Baltic Int. Symp.*, 1–6, 2008.
16. Sergievskaya, I. and S. A. Ermakov, "On wave damping due to oil films," *US/EU-Baltic Int. Symp.*, 8–13, 2008.
17. Foged, L. J., M. A. Saporetti, E. Jørgensen, T. Voigt, F. Calvano, and D. Tallini, "Measurement and simulation of reflector antenna," *9th Eur. Conf. Antennas Propag.*, 2015.
18. Boisot, O., A. Laiba, J. C. Lalaurie, and C. A. Guérin, "Dynamical properties of sea surface microwave backscatter at low-incidence: Correlation time and doppler shift," *IEEE Trans. Geosci. Remote Sens.*, 1–11, 2016.
19. Boisot, O., S. Pioch, C. Fatras, G. Caulliez, A. Bringer, P. Borderies, J. C. Lalaurie, and C. A. Guérin, "Ka-band backscattering fromwater surface at small incidence: A wind-wave tank study," *J. Geophys. Res. Ocean.*, 1–25, 2015.
20. Nunziata, F., C. R. de Macedo, A. Buono, D. Velotto, and M. Migliaccio, "On the analysis of a time series of X-band TerraSAR-X SAR imagery over oil seepages," *Int. J. Remote Sens.*, Vol. 40, 3623–3646, 2019.
21. Hara, T., E. J. Bock, and D. Lyzenga, "In situ measurements of capillary-gravity wave spectra using a scanning laser slope gauge and microwave radars," *J. Geophys. Res.*, Vol. 99, 12,593–12,602, 1994.
22. Li, X., F. Nunziata, and O. Garcia, "Oil spill detection from single- and multipolarization SAR imagery," *Compr. Remote Sens.*, 231–248, Elsevier, 2018.
23. Fan, S., V. Kudryavtsev, B. Zhang, W. Perrie, B. Chapron, and A. Mouche, "On C-band quad-polarized synthetic aperture radar properties of ocean surface currents," *Remote Sens.*, Vol. 11, 2321, 2019.
24. Elfouhaily, T. M., B. Chapron, K. Katsaros, and D. Vandemark, "A unified directional spectrum for long and short wind-driven waves," *J. Geophys. Res. Ocean.*, Vol. 102, 15781–15796, 1997.
25. Folgerø, K., "Bilinear calibration of coaxial transmission/reflection cells for permittivity measurement of low-loss liquids," *Meas. Sci. Technol.*, Vol. 7, 1260–1269, 1996.
26. Friisø, T., Y. Schildberg, O. Rambeau, T. Tjomsland, and J. Sjøblom, "Complex permittivity of crude oils and solutions of heavy crude oil fractions," *J. Dispers. Sci. Technol.*, Vol. 19, 93–126, 1998.
27. Born, M. and E. Wolf, *Principles of Optics*, 6th Edition, 613–615, Pergamon, London, 1980.
28. Zhu, C., R. H. Byrd, P. Lu, and J. Nocedal, "Algorithm 778: L-BFGS-B: Fortran subroutines for large-scale bound-constrained optimization," *ACM Trans. Math. Softw.*, Vol. 23, 550–560, 1997.
29. Nash, S. G., "Newton-type minimization via the Lanczos method," *SIAM J. Numer. Anal.*, Vol. 21, 770–788, 1984.
30. Pinel, N. and C. Bourlier, "Modeling of radar scattering from oil films," *Int. Radar Conf. Bordeaux Fr.*, Vol. 1, 1–6, 2009.
31. Pietrapertosa, C., A. Spisni, V. Pancioli, A. Pavan, P. Sterzai, P. Paganini, M. Vellico, A. Monni, and F. Coren, "Hyperspectral images to monitor oil spills in the River Po," *Boll. di Geofis. Teor. ed Appl.*, Vol. 57, 31–42, 2016.
32. Koudogbo, F., P. F. Combes, and H.-J. Mametsa, "Numerical and experimental validations of IEM for bistatic scattering from natural and manmade rough surfaces," *Progress In Electromagnetics Research*, Vol. 46, 203–244, 2004.